



1 **Observed slump of sea land breeze in Brisbane under the**
2 **effect of aerosols from remote transport during 2019**
3 **Australia mega fire events**

4 Lixing Shen¹, Chuanfeng Zhao^{1*}, Xingchuan Yang¹, Yikun Yang¹, Ping Zhou¹

5 ¹College of Global Change and Earth System Science, and State Key Laboratory of Earth Surface
6 Processes and Resource Ecology, Beijing Normal University, Beijing 100875, China

7 *Correspondence to:* Chuanfeng Zhao (czhao@bnu.edu.cn)

8 **Abstract.** The 2019 Australia mega fires were unprecedented considering its intensity and consistency.
9 There have been many researches on the environmental and ecological effects of the mega fires, most
10 of which focused on the effect of huge aerosol loadings and the ecological devastation. Sea land breeze
11 (SLB) is a regional thermodynamic circulation closely related to coastal pollution dispersion yet few
12 have looked into how it is influenced by different types of aerosols transported from either nearby or
13 remote areas. Mega fires provide an optimal scenario of large aerosol loadings. Near the coastal site of
14 Brisbane Archerfield during January in 2020 when mega fires were the strongest, reanalysis data from
15 Modern-Era Retrospective analysis for Research and Applications version 2 (MERRA-2) showed that
16 mega fires did release huge amounts of aerosols, making aerosol optical depth (AOD) of total aerosols,
17 Black Carbon (BC) and Organic Carbon (OC) approximately 240%, 425%, 630% of the averages of
18 other non-fire years. Using 20 years' wind observations of hourly time resolution from global
19 observation network managed by National Oceanic and Atmospheric Administration (NOAA), we
20 found that SLB day number during that month was only four, accounting for 33.3% of the multi-years'
21 average. The land wind (LW) speed and sea wind (SW) speed also decreased by 22.3% and 14.8%
22 compared with their averages respectively. Surprisingly, fire spot and fire radiative power (FRP)
23 analysis showed that heating effect and aerosol emission of the nearby fire spots were not the main
24 cause of local SLB anomaly while the remote transport of aerosols from the fire center was mainly
25 responsible for the decrease of SW, which was partially offset by the heating effect of nearby fire spots
26 and warming effect of long-range transported BC and CO₂. The large scale cooling effect of aerosols
27 on sea surface temperature (SST) and the burst of BC contributed to the slump of LW. The remote
28 transport of total aerosols was mainly caused by free diffusion while large scale wind field played a
29 secondary role at 500 m. Large scale wind field played a more important role in aerosol transport at 3



30 km than at 500 m, especially for the gathered smoke, but free diffusion remained the major contributor.
31 The decrease of SLB speed boosted the local accumulation of aerosols, thus further made SLB speed
32 decrease, forming a positive feedback mechanism.

33 **1. Introduction**

34 Aerosols play an important role in balancing the Earth's radiation budget, through its direct or indirect
35 effect (Albrecht, 1989; Garrett and Zhao, 2006; IPCC, 2013; McCoy and Hartmann, 2015). There are
36 different kinds of aerosols from various sources which have different climatological forcing effects
37 (Charlson, 1992; Yang et al., 2016). Aerosols differ in radiative forcing effects as their physical and
38 chemical properties vary, some of which may affect the earth-atmosphere system by bringing changes
39 to the lifespan of clouds (Albrecht, 1989; Zhao and Garrett, 2015).

40 Carbonaceous aerosol contains black carbon (BC) and organic carbon (OC) and serves as a major
41 radiation-influencing aerosol which mainly comes from biomass burning (Vermote et al., 2009, Yang et
42 al., 2021). There have been studies addressing the importance of BC on atmospheric warming and that
43 of OC on weakening *in situ* downwelling solar radiation (Jacobson, 2001; Ramana et al., 2010). There
44 were also some studies trying to quantify the average radiative forcing of BC and OC while they
45 emphasized the potential uncertainties with respect to the specific values too (Zhang et al., 2017). At a
46 planetary scale, the change of aerosols brings many uncertainties to radiation balance thus further
47 influences the magnitude of atmospheric circulation (Wang et al., 2015; Zhao et al., 2020). At a
48 synoptic scale, aerosols can affect tropical cyclone by enlarging its rainfall areas which is also related
49 to its radiative properties (Zhao et al., 2018). At a regional scale, Han et al. (2020) discussed in detail
50 the radiative forcing effect of aerosols on the speed of Urban Heat Island (UHI) during different
51 seasons.

52 As mentioned above, biomass burning is an important source of aerosols, especially for carbonaceous
53 aerosols. Adequate amounts of fire-emitted aerosols would bring perturbations to the balanced Earth's
54 climate system through both direct and indirect effects (Jacobson, 2014). There have been many
55 researches discussing the characteristics of wild fire aerosols and their effect around the world
56 (Grandey et al., 2016; Mitchell et al., 2006). For example, Portin et al. (2012) investigated the
57 characterization of burning aerosols in Eastern Finland during Russian wild fires in summer 2010.



58 Kloss et al. (2014) pointed out wild fires could have plumes ascending high and polluting remote areas
59 with the help of monsoon. Grandey et al. (2016) quantified the total fire aerosol radiative effect over
60 the globe, which is estimated to be -1.0 W/m^2 on average. The fire aerosols could have more significant
61 radiative effects with clouds than under clear sky condition through cloud-aerosol interaction, whose
62 global forcing effect could reach -1.16 W/m^2 (Chuang et al., 2002).

63 Australia is one of the areas where wild fires occur frequently (Yang et al., 2021). There are nearly
64 550,000 km² of tropical and arid savannah burnt each year in Australia, contributing to about 6%–8%
65 of global carbon emissions from biomass burning (van der Werf et al., 2006; Meyer et al., 2008).
66 Particularly, there have been many studies concentrating on wild fires' association with enhancing
67 aerosol loadings and air pollution events in Australia, some of which included the discussion of
68 combined effect from background meteorological conditions (Mitchell et al., 2006; Luhar et al., 2008;
69 Meyer et al., 2008; Mitchell et al., 2013; Mallet et al., 2017). The 2019 Australia wild fires from
70 December 2019 to February 2020 were unprecedented in recent decades in terms of its magnitude and
71 consistency so that they have attracted the attention of the world in a short time. Numerous studies
72 have been carried out since their outbreak from different aspects. For example, Yang et al (2021)
73 examined the statistical properties of aerosol properties associated with 2019 Australia mega fire events
74 in both horizontal and vertical directions. Torres et al. (2020) investigated the aerosol emissions during
75 the mega fires happening in New South Wales, Australia and found a great amount of carbonaceous
76 aerosols in the stratosphere. Ohneiser et al. (2020) traced wildfire smoke in one of the most severe
77 burnt areas in southeastern Australia and found that smoke could even travel across the Pacific, which
78 was detected by an observation site at Punta Arenas in South America.

79 Sea land breeze (SLB) is a common circulation over coastal areas whose direct cause is the temperature
80 difference between land and sea (TDLS). Many studies have investigated this regional circulation. On
81 one hand, the complicated influencing factors of SLB have been studied from different perspectives
82 (Miller et al., 2013). Our previous studies pointed out that the change of TDLS is highly related to the
83 change of *in situ* downwelling solar radiation (Shen et al., 2021; Shen et al., 2021; Shen and Zhao,
84 2020). We also found that the continuous increase of surface roughness in cities could reduce the SLB
85 speed in long term (Shen et al., 2019). The long-term significance and trends of SLBs over the globe
86 are driven by climate regimes which are related to climatological differences in both *in situ*
87 downwelling solar radiation and background wind fields. There are also many other studies on the



88 influencing factors of SLB during short periods. For example, based on the case analyses, Sarker et al.
89 (1998) found that UHI magnitude has a great impact on the encroachment range of sea wind (SW)
90 frontal surface. Using regional model simulation, Ma et al. (2013) found that UHI effect could enhance
91 TDLS a lot which would result in strengthened SLB circulation in a great metropolis. Miller et al.
92 (2013) reviewed the SLB and pointed out that local topography such as the shape of the coastline, is
93 another important influencing factor of SLB. On the other hand, SLB's effect has also been extensively
94 investigated. For example, SLB has been reported as a direct controller of air pollutants which
95 transports air pollutants inland or to the vast ocean with the help of background meteorological field
96 (Nai et al., 2018; Shen and Zhao, 2020). SLB is also essential to modify the meteorological conditions
97 and local climate (Rajib and Heekwa, 2010). Moreover, SLB is a determinant factor of the diurnal
98 variation of the precipitation on the island since its direction and magnitude can affect the location and
99 magnitude of convective systems (Zhu et al., 2017).

100 Over the years, the cause and effect of aerosols, wild fires in typical areas, and SLBs have been learned
101 in detail respectively. The relationship between aerosols and other small scale circulations such as UHI
102 circulation has also been investigated from many aspects (Han et al. 2020). However, few studies have
103 investigated the effects of different types of aerosols on SLBs or looked into how local and remote
104 aerosol loadings during mega fires would affect local SLB with the help of meteorological background
105 field or other potential mechanisms. There was an updated and important study calling for attention of
106 the record-breaking aerosol loadings during 2019 Australia mega fires which led to cooling effect to
107 ocean temperature (Hirsch and Koren, 2021). Since *in situ* downwelling solar radiation and SST, which
108 are both important influential factors of SLB, are deeply affected by the radiative effects of different
109 types of aerosols, it is interesting to examine in detail how the record-breaking mega fires would
110 influence SLB by releasing large amounts of aerosols.

111 The paper is organized as follows. Section 2 describes the observation site, data and analysis methods.
112 Section 3 illustrates the characteristics of SLB, the variation of SLB days, the distribution and fire
113 radiative power (FRP) of wild fire spots, the anomaly of observed SW speed, land wind (LW) speed
114 and air temperature, the effects of different aerosols on SLB's variation, the analysis on background
115 wind field and the comparison between local fire spots' and the remote fire center's contributions.
116 Section 4 summarizes and discusses the findings of the study and proposes a mechanism of
117 aerosol-SLB interaction during the 2019 Australia mega fires' most intense period.



118 **2. Data and methods**

119 **2.1 Site**

120 The 2019 Australia mega fires occurred mainly in the eastern and southeastern coastal areas of
121 Australian continent (Yang et al., 2021). The southeastern parts, including the State of Victoria and
122 southeastern part of the State of New South Wales, belong to Marine Climate where obvious existence
123 of SLB (OE-SLB) is not clearly verified because of the influence of strong westerlies and water vapor
124 accompanied with westerlies from the ocean (Shen et al., 2021). Note that OE-SLB means that SLB is
125 significant from a climatological perspective. In other words, the SLB can be found during most time
126 of the year. Details about the definition of OE-SLB can be found in Shen et al. (2021) and are not
127 repeated here. Meanwhile, the wild fire events were most severe with a great density according to
128 numerous reports, which could possibly cause fire-induced complex flows and circulation in the form
129 of fire-atmosphere interactions in the vicinity of a fire (Stageberg, 2018). Based on previous
130 observation during mega fire events, the concentrated fire spots changed the local air pressure field and
131 added a regional temperature-pressure field, bringing uncertainties to local wind speed and wind
132 direction (Jia et al., 1987; Li et al., 2016). On one hand, this could further interrupt the SLB formation
133 since it might make the background wind field more complicated. On the other hand, the detected SLB
134 might not be accurate since it is likely to contain other wind disturbance at a small regional scale.

135 As shown in Fig. 1, we selected an urban site in Brisbane along the eastern coast of Australia as the
136 study site, which was due to several considerations. First, while the eastern coasts of Australia belong
137 to monsoon climate, the Australian monsoon system is not strong so that the OE-SLB can be verified
138 from a climatological perspective, which also means integrated SLB circulation can be found during all
139 seasons. Second, compared to rural sites, there are longer period of high time resolution observation
140 data at urban sites, which is necessary for the extraction of SLB signals. Third, the urban area of
141 Brisbane is relatively small and is not very far from vast areas of forests which provide stable
142 combustion environment, ensuring the persistent effect of wild fires when they occur. Fourth, the UHI
143 effect, which could possibly interrupt SLB and bring errors when calculating SLB magnitude, should
144 be small for the study region considering the small scale of urban areas. Also, the wild fires near
145 suburban areas could further eliminate the UHI effect even if it could exist through their heating impact
146 on these areas. In contrast, the forest site is surrounded by or within great amounts of flora where a



147 majority of solar radiation is absorbed and scattered by leaves, prohibiting the surface heating by solar
148 radiation and then the formation and detection of SLB. Actually, due to the existence of photosynthesis,
149 the heat absorption process of leaves from solar radiation and the temperature rise of 'leave surface' are
150 different from those of Earth surface. As a result, the traditional mechanism of SLB formation is not
151 necessarily applicable when the site is in the forest or quite close to clusters of flora. Considering all of
152 these, we chose the site of Brisbane Archerfield located at eastern coast of Queensland State (Fig. 1) as
153 the study site.

154 2.2 Data

155 The Several types of data have been used in this study, including the land cover type data, the
156 Modern-Era Retrospective analysis for Research and Applications version 2 (MERRA-2) data, the
157 Moderate Resolution Imaging Spectroradiometer (MODIS) data, the ground site observation data, the
158 Fifth Version of European Centre for Medium-Range Weather Forecasts (ECMWF) ReAnalysis (ERA5)
159 data, the Firespot and FRP data, and the Global Data Assimilation System (GADS) data. The detailed
160 data information is described below one by one.

161 Land cover type data: The land cover type data of Australia is from Dynamic Land Cover Dataset
162 (DLCD) with Version 2.1 provided by Geoscience Australia. In this study, the DLCD land cover type
163 data was used to reveal the surrounding landscape of Brisbane Archerfield. The spatial resolution of the
164 data is '0.002349°×0.002349°', which is based on the annual mean of data from 2014 to 2015.

165 MERRA-2 data: MERRA-2 belongs to the global atmospheric reanalysis product managed by National
166 Aeronautics and Space Administration (NASA). It is produced by the Global Modeling and
167 Assimilation Office (GMAO) and the assimilation system of Goddard Earth Observing System
168 (GEOS-5) is used to ensure the quality of this dataset. For major ground sites over Australia, Yang et al.
169 (2021) compared its monthly aerosol optical depth (AOD) product with Aerosol Robotic Network
170 (AERONET) observations and found their RMSEs were all smaller than 0.05. Thus, MERRA-2 should
171 be reliable to be used for the analysis of the large-scale spatial distribution of AOD in Australia. Yang et
172 al. (2021) also denoted that the 2019 Australia mega fires were the strongest in January of 2020.
173 Correspondingly, we used the monthly AOD of January at 550 nm from 2002 to 2020 to check the
174 AOD difference between the mega fire year and years with no mega fires. The spatial resolution of
175 MERRA-2 AOD data is '0.625°×1°'.



176 MODIS data: The MODIS instrument is performed on Aqua and Terra platforms. In this study, we used
177 the MODIS cloud product which belongs to the dataset of MCD06COSP_M3_MODIS. The cloud
178 information includes cloud optical depth (COD) and cloud fraction for all January months during the
179 period from 2003 to 2020 with monthly time resolution. The Brisbane Archerfield site is located at
180 153.008°E , 27.57°S . So we used COD and cloud fraction data whose space range and resolution are
181 152.5°E - $153.5^{\circ}\text{E} \times 28.5^{\circ}\text{S}$ - 26.5°S and $1^{\circ} \times 1^{\circ}$ respectively. This space range covers the whole
182 Brisbane area and the normal encroaching distances of SLB which are about dozens of kilometers
183 (Rajib and Heekwa, 2010; Shen et al., 2019). In this study, the spatial averages of them were calculated
184 to represent the local COD and cloud fraction during every January from 2003 to 2020.

185 Ground site observation data: The wind and air temperature observation data are from National
186 Oceanic and Atmospheric Administration (NOAA) global observation network at the site of Brisbane
187 Archerfield (153.008°E , 27.57°S). We used data in January from 2001 to 2020 in this study. The time
188 resolution is every 3 hours at 200, 500, 800, 1100, 1400, 1700, 2000, 2300 UTC. The wind information
189 includes wind speed and direction with few missing observations. The air temperature is measured in
190 Fahrenheit and we have converted it into Celsius. The observation data was the main data used in this
191 study to show the variations of both SLB and temperature during the fire.

192 ERA5 data: The monthly mean Uwind (zonal) and Vwind (meridional) of January 2020 from the
193 ERA5 were used in this study to reveal the background meteorological field so as to assess its effect on
194 aerosol transport. The spatial resolution is $0.25^{\circ} \times 0.25^{\circ}$ at pressure levels of 1000 hPa, 975 hPa, 950
195 hPa, 925 hPa, 900 hPa, 875 hPa, 850 hPa, 825 hPa, 800 hPa, 775 hPa, 750 hPa and 700 hPa.

196 Firespot and FRP data: Firespot and FRP data are from MODIS product (MCD14). It can catch and
197 locate the active fire hotspots based on thermal anomalies of 1 km pixel resolution (Giglio et al., 2016).
198 The time resolution is daily and we used the monthly averages for January from 2002 to 2020 to look
199 into the fire situations over the years in detail.

200 GDAS data: The GADS data was used to perform the back-trajectory analysis from the Hybrid
201 Single-Particle Lagrangian Integrated Trajectory (HYSPLIT). The spatial resolution of GADS data is
202 $1^{\circ} \times 1^{\circ}$ with daily time resolution. The levels of GDADS data chosen in this study to help to perform
203 HYSPLIT analysis were 500 m and 3 km respectively. The time range set in this study was the January
204 of 2020.



205 2.3 Methods

206 2.3.1 Extracting SLB signal

207 The verification of OE-SLB and extracting of SLB signals from original wind observation over
208 monsoon areas were carried out through the method of Separation of Regional Wind Field (SRWF).
209 The definition of OE-SLB, the details of SRWF method and criterion for verification were detailed in
210 our previous studies and not repeated here (Shen et al., 2019; Shen and Zhao, 2020; Shen et al., 2021).
211 Briefly speaking, SRWF calculates the vector difference between observed wind vector and daily
212 average wind vector for each observation time. Then, the vector difference is considered as the local
213 wind. The criterion of OE-SLB requires that there exist intersection sets among the range of SW, the
214 range of LW and the range of hourly average of wind angle in a diurnal period (HAWADP). Also, the
215 intersection set between the range of SW (LW) and the range of HAWADP only exists during daytime
216 (nighttime). Then the local wind can be thought as the SLB signal as long as the OE-SLB is verified at
217 that site. Based on HAWADP and specific sea-land distribution, we further defined the prevailing time
218 of sea wind (PTS) and prevailing time of land wind (PTL). Briefly speaking, during PTS (PTL) the
219 local wind keeps blowing from sea (land) and the wind angle keeps rotating towards the direction of
220 vast sea (inland). The HAWADP at Brisbane Archerfield is shown in Fig. 2. As shown, the HAWADP
221 of local wind was close to sinusoid, which conformed to previous findings in other monsoon areas
222 (Shen et al., 2021; Yan and Anthes, 1987). According to the sea-land distribution shown in Fig. 1, we
223 first defined the ranges of SW and LW and then the OE-SLB of Brisbane Archerfield was verified
224 using these criteria. We further selected the PTS (PTL) based on the rules above.

225 To make it clear, we summarized the range of SW, LW, PTS and PTL in Table 1. Note that the actual
226 PTS (PTL) may be longer than what we defined here because the time resolution is 3 hours instead of
227 hourly in this study. As a result, we cannot know the exact threshold of time when the wind angle meets
228 the criteria mentioned above. For instance, it is possible that the wind angle is within the range of SW
229 before 0500 UTC. However, it is still sure that the SW (LW) develops vigorously during 0500-0800
230 UTC (1400-2000 UTC) based on Fig. 2, which means that ‘0500-0800 UTC’ and ‘1400-2000 UTC’ are
231 within the real PTS and PTL respectively even if they are not the exact PTS or PTL. Thus, the defined
232 PTS (PTL) in this study is reliable. The aim to define PTS (PTL) is to find the time period when SW
233 (LW) develops most vigorously so as to ensure further exclusion of winds from synoptic scales when



234 extracting real SLB signals after applying the SRWF method (Shen and Zhao, 2020; Shen et al., 2021;
235 Cuxart et al., 2014).

236 **2.3.2 Definition of the SLB day**

237 SLB day is the day when SLB circulation is most significant (Xue et al., 1995). To some extent, the
238 number of SLB days reveals the activity level of SLB. Different criteria have been adopted when
239 defining SLB day. Here we referred to our previous study (Shen et al., 2019) to adopt the criteria based
240 on the minimum times of successful detection of winds coming from the range of SW (LW) during
241 PTS (PTL). Since the time interval between two adjacent observations is 3 hours, which makes the
242 total observation hours less than the total hours during prevailing time, we modified the criteria slightly
243 as follows: when the offshore land winds occur in the time period of 1400-2000 UTC with total
244 occurrence time no less than 3, and the onshore sea winds occur in the time period of 500-800 UTC
245 with total occurrence time no less than 2, the day is counted as a SLB day.

246 **2.3.3 The calculation of monthly SW and LW speeds**

247 After defining PTS, PTL and SLB day, we could finally calculate the monthly SW and LW speeds.
248 First, we picked up SLB days in every January from 2001 to 2020. Second, we picked up local wind
249 speed during PTS (PTL) on SLB days and calculated the monthly average of SW (LW) speed in every
250 January from 2001 to 2020.

251 Based on GDAS data throughout the whole January in 2020, the back trajectories of lower atmosphere
252 at Brisbane Archerfield were simulated using the HYSPLIT model. This could help analyze the
253 transport effect of background wind fields on aerosols at this site. The simulated levels at the site were
254 500 m and 3 km since the lower level of atmosphere (500m) was closer to fire spots and there was also
255 accumulated smoke at 3 km in the southeastern parts of Australia during the exact same month (Yang et
256 al., 2021). The TrajStat module of Meteoinfo version 2.4.1 was also used to cluster the back trajectories
257 based on the Euclidean distance method, whose details and source code could be found at its official
258 website (<http://meteothink.org/docs/trajstat/index.html>, last access: 31 January 2021).

259 **2.3.4 The calculation of monthly temperature during daytime and nighttime**

260 After defining the SLB day, PTS and PTL, we calculated the monthly temperature during daytime and
261 nighttime using the similar method as SW and LW speeds. First we selected the temperature on SLB



262 days. Second, we calculated the monthly average of temperature during PTS (PTL) to represent
263 monthly average temperature during daytime (nighttime) in January. Actually, temperature during
264 daytime (nighttime) represents land temperature when SW (LW) prevails. In order to make it clear and
265 concise, we call it temperature during PTS (PTL) or land temperature during daytime (nighttime) in
266 this study.

267 3. Results

268 3.1 The variation of SLB day number

269 Figure 3 shows the SLB day number in January from 2001 to 2020. As shown, the SLB day number in
270 January was normally larger than 10. Among these 20 years, there were 25% of the years whose SLB
271 days in January accounted for more than half of the month. Note that it does not necessarily mean that
272 there is no SLB on days that are not SLB days. It is obvious that there was a slump in the number of
273 SLB day in 2020. The total SLB day number dropped to only 4 during the mega fire events, accounting
274 for only 33.33% of the average SLB day number during the past 20 years. Also, year 2012 also
275 witnessed low SLB day number (6 days) in January. There are a lot of potential influencing factors for
276 SLB frequency, such as the background wind field (Miller et al., 2013) and the interruption of other
277 small scale circulations (Kusaka et al., 2000). Among all the influencing factors, cloud is one of the
278 most important because it has significant effect on *in situ* solar radiation which is the direct cause of
279 TDLS. We would discuss this in the following sections.

280 3.2 The trends in SW and LW speeds and local air temperature

281 The monthly mean SW and LW speeds in January are shown in Figure 4a. As can be seen, there were
282 fluctuations of both SW and LW speeds in January from 2001 to 2020. The SW speed was higher than
283 LW speed, which conformed to many previous findings (Miller et al., 2013; Zhu et al., 2017). The
284 averages were calculated as 3.70 m/s for SW speed and 2.86 m/s for LW speed, respectively. Figure 4b
285 and c show the anomalies for both SW and LW speeds. In general, LW speed fluctuated more
286 significantly than SW speed did. This is due to its lower level of kinetic energy which could make it
287 more sensitive to any potential interruptions from the background meteorological field (Shen and Zhao,
288 2020). The negative anomalies of LW speed happened in 2001, 2004, 2008, 2010, 2011, 2015, 2016,
289 2017, 2018 and 2020. Different from other years, it is obvious that the negative anomaly in 2020 was



290 higher than 0.6 m/s, which was beyond the multi-year oscillation range. The anomaly accounted for
291 22.3% of multi-years' average LW speed. The negative anomalies of SW speed happened in 2004, 2008,
292 2009, 2010, 2011, 2013, 2014, 2015, 2017 and 2020 (Figure 4c). For SW speed, the negative anomaly
293 value in 2020 was also obvious but it was still within the multi-year oscillation range. It was higher
294 than 0.5 m/s, accounting for 14.8% of the multi-years' average. It is interesting to find that there were
295 obvious positive anomalies of both SW and LW speeds in 2003 whereas their absolute values were not
296 the highest. Also, the SLB day number in 2003 was near the average. We will further discuss this along
297 with the aerosol emissions during that year in the following sections.

298 It can be seen in Figure 4b that there were also significant fluctuations in nighttime land temperature
299 over the years. There was a soar in land temperature in 2020 which approached nearly 24 °C. It was
300 nearly 3 °C more than the multi-years' average, exceeding the range of multi-years' oscillation. The
301 fluctuation of land temperature during daytime was less significant than that during nighttime. There
302 was obvious positive anomaly in 2020, indicating that the daytime land temperature was higher than
303 those in normal years. Meanwhile, it was still within the range of multi-years' oscillation range though
304 the positive anomaly was obvious. Fire spots have heating effect on the nearby environment through
305 either shortwave radiation of light from fires or heat conduction caused by temperature gradient. It can
306 be inferred that mega wild fires during January 2020 contributed to the positive temperature anomalies
307 during PTS (PTL) through the heating effect of fires though it might not be the only cause. The heating
308 effect during fire events was more significant during nighttime than daytime. This is probably due to
309 colder background temperature field during nighttime.

310 Basically, the decreased SW (LW) speed revealed that the TDLS during PTS (PTL) decreased. To be
311 more specific, the temperature difference between the small regions where the upward stream and
312 downward stream of SLB circulation lie respectively became smaller during January 2020. Based on
313 Figure 4b and c, temperature during PTL seems to be negatively related to LW speed anomaly while it
314 is obvious that temperature during PTS does not show any corresponding relationship with SW
315 anomaly.

316 In order to be more accurate, we carried out linear regression between temperature during PTL and LW
317 anomaly and found that they had negative linear relationship ($p < 0.02$) with each other (Figure 5). As
318 the temperature increased by 10 °C, the LW speed anomaly decreased by 1.52 m/s. During nighttime,
319 the land is colder than the sea. As the land temperature increases, the TDLS becomes smaller if the SST



320 where the upward stream of SLB lies remains relatively stable, so does the LW speed. Shortly, the good
321 linear relationship reveals that the variation of temperature during PTL (nighttime land temperature)
322 could generally represent the variation of TDLS during PTL while the daytime land temperature
323 variation could not represent the TDLS variation during PTS. In our previous study, we also found
324 through observation that the daily lowest temperature (DLT) was well negatively related to LW speed
325 while the SW speed was more related to in situ solar radiation rather than merely land temperature
326 (Shen et al., 2021), which was similar to the findings here. It could be inferred that although the land
327 temperature during daytime increased during mega fire events, TDLS was still narrowed during fire
328 events. If we only consider the land temperature, the SW speed should have increased during fire
329 events because SW circulation is formed due to warmer land and colder sea. Consequently, there
330 should be other factors which could cause decreased TDLS during PTS, which is the direct cause of
331 SW speed decrease. We would investigate this in the following sections.

332 **3.3 The distribution and FRP of fire spots**

333 Since the heating effect depends largely on the distance between the area heated and the heat center, it
334 is necessary to examine the distribution of fire spots in January over the years, which is shown in
335 Figure 6. It can be seen that fire spots scattered all over the eastern part of Australia over the years
336 during January. January is the middle of Australian summer which is the season when wild fires are the
337 most frequent (Yang et al., 2021). Apart from 2020, other years also witnessed considerable scattered
338 fire spots all over the coastal and inland regions. It is obvious that there was an extreme fire center in
339 the southeastern corner of Australia with great density of fire spots in January 2020. This was exactly
340 the region where the 2019 Australia mega fires mainly happened. To be specific, it was the eastern
341 corner of Victoria State and the southeastern corner of New South Wales State, which conformed to
342 many reports from media. There was also a great fire center in the southeastern corner in 2003 although
343 the scale was smaller than that in 2020. Considering the distribution of fire spots near the site, the
344 density of fire spots nearby was not higher than in other years. Instead, there seems to be more fire
345 spots nearby the site in 2003, 2005, 2006, 2010 and 2013 in the figure. If we restrained the nearby
346 region to areas with smaller scale, year 2003 and 2013 rather than 2020 had the most nearby fire spots.
347 There exists another possibility that although the fire spots nearby the site were not more concentrated
348 with great density in 2020 than in other years, the FRP of fire spots in 2020 was higher. This means that



349 the fire was greater regardless of the ordinary density of spots, which could result in more fire aerosol
350 emissions. So we further examined the FRP of fire spots in 2020 and in other years. In order to make it
351 comparable and verifiable, the time period of data chosen here was the same as that in Figure 6. As
352 shown in Figure 7a, both the nearby and local fire spots in 2020 were mostly within the lowest FRP
353 range, which was less than 235 MW. There were some sparse fire spots with greater FRP (235-863
354 MW) scattered all over the eastern part of Australia. The FRP of the fire center was higher than the FRP
355 of other fire spots where there were many fire spots with greater FRP which belonged to the range of
356 '235-863 MW' or '863-2194 MW'. Figure 7b shows the FRP of all fire spots from 2002-2019. The
357 FRP of nearby or local fire spots were also with the lowest values. With the year number increased, the
358 density of fire spots with higher FRP (235-863 MW) increased significantly, most of which were
359 located at inland areas of Australia continent. This indicates that scattered wild fires with low or
360 medium FRP are common in Australia but concentrated mega fires are not so common. There were also
361 some fire spots which belonged to the range of '235-863 MW' or '863-2194 MW' in 2003, yet the
362 number was less and the distribution areas were smaller. Based on Figure 7, one important point we
363 found is that there was no discrepancy between FRP of nearby or local fire spots in 2020 and that of
364 nearby or local fire spots in other years. So the possibility mentioned above was discarded.

365 Based on the analysis above, the nearby fire spot density and FRP in 2020 were both at the same level
366 as other years for local regions near the site. This implies that the heating effect of nearby fire spots did
367 exist in 2020, contributing to the increase of land temperature to some extent, but it was not likely the
368 major cause of land temperature anomaly. Fluctuation of land temperature might be caused by
369 combined mechanisms or some other potential factors. In other words, the heating effect of fire spots
370 does not necessary correspond to observed air temperature increase. For example, Figure 4b and c
371 show that there were negative land temperature anomalies in 2003 but actually this year witnessed
372 greater density of nearby or local fire spots. In real situation, the scale of SLB is quite small. The fire
373 spots might be quite a long distance away from the area where vertical stream of SLB lies as a result of
374 which the heating effect is weak.

375 **3.4 The spatial distribution of aerosols**

376 Large fires would have great aerosol loadings which would affect the *in situ* solar radiation and then
377 the radiation budget. Based on the basic physical mechanism of SLB formation, the observed decreased



378 SW and LW speeds demonstrated the decreased TDLS. As mentioned above, the heating effect of
379 nearby fire spots was weak and did not become more significant in 2020. So the more important factors
380 bringing about the decrease of SW and LW speeds should be closely related to TDLS rather than the
381 land temperature only. The TDLS during SLB formation is highly related to the *in situ* downwelling
382 solar radiation. As the shortwave radiation increases, the TDLS becomes larger due to the different heat
383 capacities of land and sea. SW forms and prevails when TDLS is enough to drive the thermodynamic
384 circulation. During nighttime, the land-sea system is the heater for upper atmosphere as they both gives
385 out heat and undergoes energy loss in the form of longwave radiation. As the outgoing longwave
386 radiation increases, the TDLS also becomes larger due to the different heat capacities of land and sea.
387 Then the LW forms in the similar way as SW forms.

388 Based on discussions above, *in situ* downwelling solar radiation is a crucial factor for SW speed.
389 Considering that aerosol is an important factor affecting *in situ* downwelling solar radiation, it is
390 necessary for us to check the temporal and spatial variations of aerosols over the years. Figure 8 shows
391 the spatial distribution of AOD of total aerosols (TA-AOD) over the years using MERRA-2 aerosol
392 product. Over the years, the background level of TA-AOD was generally low in Australia, implying
393 that Australia was less polluted from human pollution. The TA-AOD in 2020 increased significantly
394 compared with the average level. It can be seen that there was a maximum value center in the southeast
395 corner, which overlapped the region of fire spots center (Figure 6). The peripheral area of maximum
396 value center was covered with isopleth showing the characteristics of free diffusion of aerosols in the
397 air. There was also a maximum value center in 2003 whose scale was smaller, overlapping the smaller
398 region of fire center in 2003. Based on findings from these three aspects, it can be concluded that the
399 mega fire center was the main source of large aerosol amounts around the site location. In general, the
400 TA-AOD was about 240% of the multi-years' average level at the site, while the TA-AOD in the fire
401 center was at a more astonishing level, accounting for more than 420% of the multi-years' average
402 level at the site. Aerosol could significantly affect the *in situ* downwelling solar radiation through direct
403 radiative forcing. Turnock et al. (2015) calculated the relationship between AOD and surface solar
404 radiation (SSR) and found that when the background value is low over the years, the SSR increases by
405 10% as AOD varies from 0.32 to 0.16. In this study, the TA-AOD increased even more significantly
406 (240%) considering the low background value. Normally, when we talk about the radiative forcing of
407 aerosols in the form of SSR difference, it means instantaneous radiative forcing. However, the



408 formation of SLB is the result of different levels of radiation accumulations between land and sea. So
409 the effect of aerosols on the total *in situ* downwelling solar radiation can accumulate in the process of
410 SLB formation and results in even more significant impacts on the change of surface temperature.
411 Apart from aerosols, clouds could play an even more important role in the radiation budget. The COD
412 and cloud fraction anomaly at this site are shown in Figure 9. The time range was from 2003 to 2020
413 due to data availability. It can be seen that both the cloud fraction and COD in 2003 were at an obvious
414 low level, while both the cloud fraction and COD in 2020 showed a tiny negative anomaly. Based on
415 the spatial distribution of TA-AOD, both 2003 and 2020 witnessed a soar in TA-AOD at the site while
416 TA-AOD increased more significantly in 2020. Figure 3 shows that there was a slump in SLB number
417 in 2020 while not in 2003, while Figure 4 shows that there were positive anomalies of both SW and
418 LW speeds in 2003. Many previous studies on SLB have pointed out that high level of *in situ*
419 downwelling solar radiation is favorable for SLB formation and SLB speed increase (Shen and Zhao,
420 2020; Shen et al., 2021, Miller et al., 2013). Our previous study in monsoon climate region also showed
421 that there was a positive linear relationship between *in situ* downwelling solar radiation and SW speed
422 (Shen and Zhao, 2020). As known, the *in situ* downwelling solar radiation is determined by both cloud
423 and aerosols through their combined ‘Umbrella Effect’. The finding shown in Figures 3 and 4 could be
424 explained by the radiative cooling effects of aerosols and clouds. Although there was positive anomaly
425 of TA-AOD in 2003, the COD and cloud fraction was less than the average, offsetting the aerosols’
426 negative radiative forcing effect. *In situ* downwelling solar radiation of the regional sea-land system
427 was still ensured so that the SLB happened with a normal frequency (Figure 3) and with an even larger
428 speed (Figure 4). The *in situ* downwelling solar radiation in January 2020 should be lower than the
429 average, considering the tiny negative anomaly in both COD and cloud fraction and the significant
430 increase in TA-AOD. The increased radiative forcing effect of TA-AOD was accumulated during the
431 formation of SW. In conclusion, during daytime, the negative radiative forcing effect of total aerosols
432 was the determinant factor to weaken the *in situ* downwelling solar radiation, resulting in lower level of
433 TDLS and then decreased SW speed.

434 Mega fire events are special in emitting large amounts of carbonaceous aerosols which include OC and
435 BC. The OC is a very good scatter to solar radiation. Thus, among all the aerosols, OC could be an
436 important contributor of the weakened TDLS during SW formation. Figure 10 shows the spatial
437 distribution of OC over the years. The spatial distribution of OC was also similar as the fire spot



438 distribution, which further confirmed that the source of great aerosol emissions was from mega fire
439 events. There were extreme value centers in the fire center in both 2003 and 2020. Same as found
440 earlier, it can be seen that the large value spread to farther place in 2020 than 2003, indicating that the
441 fire events were more severe in 2020 than 2003. Similarly, the background value of OC at the site was
442 low on average. The specific value of OC-AOD at Brisbane site in 2020 was about 630% of the
443 multi-years' average, which was even higher than that of total aerosol. This is easy to understand
444 because the fire center is also covered with plants and trees and the combustion of them can bring
445 significant amounts of carbonaceous aerosols. Zhang et al. (2017) estimated the radiative forcing of OC
446 globally using BCC_AGCM2.0_CUACE/Aero model, which showed that Brisbane was within the
447 large value area with high levels of negative radiative forcing at the top of atmosphere. They also owed
448 this to biomass combustion. Thus, both total aerosol and OC made great contributions to SW speed
449 decrease by decreasing *in situ* downwelling solar radiation in January 2020.

450 The result above is analyzed based on the impacts of aerosols on solar radiation. However there is
451 almost no shortwave radiation during nighttime. Then one question pops up: why was the slump of LW
452 speed more significant, which indicated that the TDLS was significantly weakened at night in January
453 2020? While the heating effect of fire spots on nighttime land temperature did exist which was more
454 significant than that during daytime, it was not likely the main cause of weakened TDLS based on FRP
455 and fire spot distribution analysis. We next checked the spatial distribution of BC over the years in
456 Figure 11. It shows that BC-AOD at the site was about 425% of the multi-years' average level with the
457 extreme value center overlapping the area of that of fire spots density. Similar as the distribution of
458 TA-AOD and OC-AOD, the peripheral areas of maximum value center are covered with isopleth
459 showing the characteristics of free diffusion. BC is well known as a kind of absorbing aerosols which is
460 reported to have wider range of absorbing band than greenhouse gases, which can absorb broadband
461 radiation from visible light to infrared wavelength (Zhang et al., 2017). During daytime, it can absorb
462 solar radiation, longwave radiation from the warmer land, and shortwave radiation from local fires.
463 During nighttime, it has a warming effect on both atmosphere and Earth surface through longwave
464 radiation. As a result, it has a warming effect on the Earth-atmosphere system including the surface of
465 the regional land-sea system so that there was a temperature soar shown in Figure 4b. The soaring BC
466 during the mega fire heated the local atmosphere, which was like adding a 'heater' in the air. The
467 'heater' then gave out downward longwave radiation to the regional land-sea system. Just like the sun



468 during daytime, this could trigger a SW circulation anomaly, weakening LW circulation. Considering
469 the BC burst during mega fire events, it is nothing weird about its dominant role in local land
470 temperature increase. The mechanism proposed above can be summarized as follows. During nighttime,
471 the formation of LW originates from the process of heat release of both land and sea. As they both lose
472 heat with different paces due to different heat capacities, the TDLS is enlarged. During the mega fire
473 event, the upper atmosphere of the regional land-sea system is heated so that the vertical temperature
474 gradient is weakened, which is unfavorable for heat release of both sea and land surfaces. As a result,
475 the TDLS is significantly weakened.

476 Another potential contributing accelerator is CO₂ which is also the product of fires due to the
477 combustion of plants and trees. CO₂ is a kind of greenhouse gas which is likely to be engaged in the
478 same mechanism as BC to reduce TDLS during nighttime except that CO₂ cannot affect the
479 downwelling solar radiation. Details about this is not repeated again. However we should note that the
480 effect of CO₂ is based on theoretical analysis rather than observational verification due to the lack of
481 accurate observation data. Both BC and CO₂ reduce TDLS, which partially offset the enhanced
482 radiative forcing effect of total aerosols, but their combined warming effect is more significant during
483 nighttime than during daytime. That is most likely the reason (at least partially) that SW speed had
484 negative anomaly but was less significant than LW speed.

485 What we discussed above are all factors whose influences were restrained to a small scale. Although
486 SLB is a small scale system, it can still be affected by the variations of signals in a large scale, since the
487 local temperature is affected by both regional forcing and the variation of large scale background
488 temperature field. In our previous study, we weighed their contributions qualitatively (Shen et al.,
489 2019). We here simply discuss the potential change in large scale SST. Hirsch and Koren (2021)
490 warned the effect of record-breaking aerosol emission from this mega fire on cooling the oceanic areas.
491 On a large scale, its average radiative forcing on sea surface was $-1.0 \pm 0.6 \text{ W/m}^2$. The temperature
492 decrease of large scale sea surface could have negative forcing on the SST at a regional scale, though
493 the specific temperature variation of the sea surface where the SLB vertical stream lies might not be the
494 same.

495 We summarized all the influencing factors of TDLS at both regional and large scales in Table 2. Among
496 all these factors, aerosols, BC, OC and CO₂ had direct forcing on TDLS by changing the solar radiation
497 reaching the regional sea-land system. In contrast, heating effect of fire spots and large scale SST



498 signal had forcing on land temperature and regional SST respectively thus further had different forcing
499 effects on TDLS during daytime and nighttime. During 2019 Australia mega fires, TDLS during
500 daytime and nighttime both decreased under their combined forcing effects, which could be inferred
501 from the anomalies of SLB speed. Clearly, the directions of all forcing effects from different factors
502 were the same during nighttime. That was why LW speed decreased much more significantly than SW
503 speed did. The negative radiative forcing of total aerosols was the determinant cause for TDLS
504 decrease during daytime, which could only be partially offset by other factors.

505 **3.5 Source of aerosols**

506 **3.5.1 Fire center's emission**

507 As indicated earlier, year 2020 did not have advantages over other years in terms of local and nearby
508 fire spot density and FRP during January. Note that certain land cover type could also increase the
509 aerosol emissions. For example, if there were more combustible such as forests or plants, the fires
510 could emit more carbonaceous aerosols in form of smoke. Considering this possibility, we further
511 checked the latest version of land cover in Australia online
512 (<http://maps.elie.ucl.ac.be/CCI/viewer/index.php>). It was updated to 2019 which overlapped with the
513 starting time of 2019 Australia mega fire events. It showed that the areas and density of flora near the
514 site were stable over the years, implying that the soar in local aerosols during mega fire events was not
515 likely caused by the change of land cover either.

516 As Figures 6-8 and 10 show, the distributions of fire spots, TA-AOD, BC-AOD and OC-AOD were
517 quite similar as each other. In the fire center, both the density and FRP of fire spots were much higher
518 in January 2020 than in January of other years. These are all based on distribution characteristics at a
519 large scale. In order to show the fire situation at the fire center more accurately, we magnified the FRP
520 map to restrain the areas to merely the fire center, which is shown in Figure 12. As shown, the fire spot
521 density was quite high in this area, especially along coastal areas. Compared with other areas, the fire
522 center had much more fire spots with higher FRP. The spots with FRP from 235 to 864 MW were
523 evenly distributed in all fired areas, surrounded by low FRP spots with high density. There were quite a
524 few spots with even higher FRP ranging from 864 to 2,194 MW, which could not be found in other
525 periphery areas (Figure 7a). In some areas at the fire center, we could even find fire spots with FRP
526 ranging from 2,194 to 5,232 MW. All these distribution characteristics of fire spots suggest the



527 possibility of large amounts of aerosols including smoke being emitted to the atmosphere, after which a
528 great concentration gradient in the horizontal direction formed between the fire center and farther areas.
529 Based on the basic Chemistry law, irreversible free diffusion would happen in this process. As the
530 concentration gap increases, the diffusion efficiency also increases. The distribution of contour lines in
531 Figures 8, 10 and 11 also shows the characteristics of free diffusion. Similar mechanism works out for
532 the spatial distribution of CO₂ during the fire events.

533 3.5.2 Analysis on the background wind field

534 Apart from free diffusion, wind is crucial for pollution transport including aerosols (Walcek, 2002).
535 Also, wind is a key factor influencing the near-surface CO₂ distribution (Cao et al., 2017). Zhang et al.
536 (2017) confirmed that BC could be transported through a long distance in mid-latitude areas. The
537 transport distance of OC was even longer than that of BC. It is necessary for us to look into the
538 background wind field in order to know the likely aerosol transport from the fire center to the site.
539 Yang et al. (2021) retrieved the average status of the vertical distribution of various aerosols in
540 southeastern Australia during 2019 Australia mega fires and found most of them accumulated under 3
541 km, which is about 700 hPa. Figure 13 shows the monthly average of background wind field based on
542 wind information at pressure levels from 1000 hPa to 700 hPa during January in 2020. The red cross
543 symbols represent the fire spot in this figure. The average background wind field clearly revealed the
544 existence of southern hemisphere's westerlies and subtropical high. The fire center was approximately
545 located at the intersection of the northern boundary of westerlies and southwestern boundary of
546 subtropical high. Since January is the middle month of Australian summer, the subtropical high
547 developed quite vigorously, some of which stretched into the eastern part of Australian continent. It
548 covered the areas where most fire spots were located. At a large scale, this brought quite hot and dry
549 background meteorological field, which was favorable for the development and persistence of wild
550 fires. Based on the average status of wind fields at different pressure levels, the subtropical high and
551 westerlies together formed a background wind field blowing from the site to fire center, which was not
552 favorable for the aerosol transport from the fire center to the site. However, we should notice that this
553 figure merely describes the monthly average status but ignores the status of wind flows at a more
554 accurate fine time scale. In other words, it is still possible that aerosols from the fire center were
555 transported to the site within some short periods in January 2020, thus made contribution to the positive



556 aerosol anomaly shown in Figures 8, 10 and 11. Based on the specific dates of SLB day during mega
557 fires identified in previous section, which were 4th, 14th, 20th and 28th in January respectively, we
558 divided the January in 2020 into five short time periods by excluding the identified SLB days. These
559 five short time periods were all named as ‘No-SLB period’. We did the backward trajectory analysis
560 during each No-SLB period to see if the aerosols from the fire center were transported to the site with
561 the help of background wind field, thus further made this period a ‘No-SLB period’ through all the
562 mechanisms mentioned above. It is easy to understand that the near surface concentration of aerosol
563 should be at a high level in general not only because it was near the fire spots but also because it is
564 within boundary layer. Considering these aspects, the backward trajectory analysis was carried out at
565 500 m over the site. Figures 14a-e show the wind backward trajectories at this site during the five
566 No-SLB periods respectively. During the No-SLB periods of a, c, d and e, the winds mainly came from
567 the southern Pacific to the east of Australia continent, which could not transport aerosols from the fire
568 center. There were winds coming from the fire center merely during period b. The northern edge of
569 wind flow beam was quite near the fire center, then it went further towards the northeastern direction in
570 the southern Pacific. When it reached the general position of subtropical high, it turned back to the
571 direction of northwest before finally reaching the site. The high pressure gradient between the center
572 and edge of the subtropical high was opposite to its moving direction, which might be the cause of its
573 abrupt turning. Although the southwestern edge of the subtropical high itself had wind flows whose
574 directions were away from the Australia continent at a monthly average (Figure 13), the wind flows
575 from northern edge of southern hemisphere’s westerlies could still move along its southwestern edge as
576 soon as they intersected with each other if smaller time scale and single level were considered (Figure
577 14b). Figure 14f showed the contributions of main backward trajectories based on the whole month’s
578 statistics. It can be seen that the wind flows which could potentially bring aerosols from the fire center
579 still had a little contribution, which accounted for 9.32% (2.87%+6.45%). In contrast, winds coming
580 from the Pacific to the east and northeast of the Australia continent dominated the wind field at the site,
581 whose contributions were 25.09% and 54.12% respectively. Thus, the aerosol contribution from wind
582 transport should be limited, which was only found during one time period with time length less than 10
583 days in January 2020. From the perspective of multi-layers of atmosphere (0-3 km), the multi-layers of
584 background wind fields as a whole did not contribute to the aerosol and CO₂ transport from the fire
585 center to the site. Therefore, the soar of aerosols including BC and OC at the site should be mainly



586 caused by the combined effect of combustion in the fire center and great free diffusion caused by
587 significant concentration gradient, with likely relatively weak contribution of the wind transport.

588 Most aerosols are generally within atmospheric boundary layer under normal conditions while it might
589 be different under the situation during mega fire events considering the boost of vertical movement due
590 to great heat release from fires and astonishing amounts of aerosol loadings. Smoke, as a kind of
591 unique aerosol loading with great amounts during fire events, could be essential to SW and LW speed
592 anomaly due to its absorptive radiative properties, making it particularly valuable to examine its
593 transport individually. Yang et al. (2021) analyzed the vertical distribution of smoke on southeastern
594 parts of Australia, which included the fire center and the site, and found that the smoke accumulated at
595 3 km generally. Considering this, we also did the backward trajectory analysis at 3 km whose time
596 division was the same as that at 500 m. The results are shown in Figure 15. As shown, the wind flow
597 scattered more evenly at 3 km than at 500 m. There were more wind flows coming from the
598 southwestern direction of the site. This is probably due to the fact that the magnitude and stretching
599 area of westerlies are larger at upper atmosphere than at layers closer to the surface. During period a, b
600 and e, there were clusters of wind flows coming from the fire center or near the fire center, which could
601 bring aerosols to the site. Specifically, there were wind flows penetrating the fire center directly during
602 period a and e, while the wind flows during period b are only adjacent to the north edge of fire center.

603 Since the period b was the longest among all No-SLB periods, it did not necessarily mean that the
604 wind's aerosol transport effect during this period was less than those during other periods although the
605 wind flows were not directly from the fire center. The moving paths of them were similar as that of
606 wind flows in Figure 14b, which all had an abrupt turning on the Pacific to the southeast of the site.

607 This is probably because that the south hemisphere's subtropical high developed to be quite strong
608 during the middle of summer, making the pressure gradient exist both at 500 m and 3 km. Figure 15f
609 shows the contribution of wind flows on monthly average, whose clustering number was also four.

610 There were four main directions of wind flows, whose contribution were 28.67%, 21.86%, 11.47% and
611 37.99% respectively. In order to make it clear, we define these four main wind flows as wind flow
612 clusters. The wind flow clusters with contributions of 21.86% and 11.47% were generally adjacent to
613 the north edge of the fire center, which contained contribution of wind flows from the fire center. Due
614 to the clustering limitation of Meteoinfo, we could not extract the specific contributions of wind flows
615 blowing directly from fire center from the total contributions of wind flow clusters (21.86% and



616 11.47%). But based on analysis on shorter time periods, their contributions were larger than those at
617 500 m because there were more No-SLB periods with wind flows blowing from fire center.

618 **4. Summary and discussion**

619 This In this study, the SLB day number, SLB speed, daytime temperature and nighttime temperature at
620 Brisbane Archerfield during January were calculated from 2001 to 2020 using observation data from
621 automatic meteorological station. We have taken three steps in total to exclude the interference of
622 winds from synoptic-scale systems in order to extract the real SLB signals. First, we used SRWF
623 method to verify the OE-SLB and then extracted the SLB signal from original observation. Second, we
624 defined SLB day when the whole SLB circulation is most significant and integrated. Finally, we used
625 SLB signals during PTS (PTL) on SLB days to calculate the monthly average of SW (LW) speed.
626 During the corresponding month over the years, regional cloud fraction, COD, fire spot and FRP
627 distribution in Australia were revealed using MODIS product. Aerosol distributions in eastern Australia
628 were revealed in the form of AOD using MERRA-2 product, including that of total aerosols, OC and
629 BC. Furthermore, the background wind field and backwards wind trajectory were analyzed by ERA5
630 product and HYSPLIT respectively. The main findings of this study are as follows.

631 1). There was a significant slump in SLB day number (33.3% of the average level) and LW speed
632 (decreased by 22.3% of the average level) at the site. While SW speed also decreased by 14.8% of the
633 average level, it was not significant.

634 2). There was a burst of aerosols at the site, with TA-AOD, BC-AOD and OC-AOD approximately
635 240%, 425%, 630% of the multi-years' averages. TDLS is the direct cause of SLB while other factors
636 influence SLB through their effects on TDLS. The variation of nighttime land temperature could
637 generally represent the variation of TDLS during nighttime while TDLS during daytime could not be
638 simply represented by daytime land temperature. Specifically, the significant aerosol burst was mainly
639 responsible for the decrease of SW speed. The burst of BC at the site as well as the large-scale SST
640 decrease during mega fires were mainly responsible for the slump of LW speed. CO₂ emitted by nearby
641 fire spots or transmitted from the fire center was a potential and weak factor for the slump of LW speed.
642 While the heating effect of nearby fires on TDLS was weak during both daytime and nighttime.

643 3). Emissions from fire center were mainly responsible for the local positive aerosol anomaly during



644 mega fire events. On average, the background wind fields from near surface to 3 km were not favorable
645 for aerosol and CO₂ transport. But there were likely aerosol and CO₂ transports through large scale
646 wind field at single level during shorter periods within January of 2020. Specifically, the wind flow
647 transport at 3 km was stronger than that at 500 m, which was particularly important for smoke transport
648 since the smoke from fires gathered at the same level. In general, free diffusion due to large
649 concentration gradient was mainly responsible for aerosol transport and the potential CO₂ transport
650 while the effect of background wind field played a second role.

651 In order to make it clear and concise to the influencing factors of SLB, we summarized their potential
652 mechanisms in local sea-land system (Figure 16). During daytime, negative anomaly of SW speed was
653 found at the site during January in 2020 when Australia mega fires were most intensive. The local
654 cloud fraction and COD were almost on an average level while there were much more aerosols during
655 mega fire events, which mainly came from fire center by free diffusion. They significantly weakened
656 the *in situ* downwelling solar radiation thus further narrowed the TDLS, which was the direct cause of
657 SW speed decrease. BC and CO₂ heated the atmosphere and warmed the earth-atmosphere system by
658 longwave radiation from the heated atmosphere. Warming effect of BC and CO₂, the decrease of SST at
659 a large scale and the weak heating effect of nearby fire spots partially offset the effect of aerosols on
660 narrowing TDLS, making the negative SW speed anomaly not exceed the multi-years' oscillation range.
661 During nighttime, the heating effect of nearby fire spots was still weak but more significant than that
662 during daytime. The warming effect of BC and CO₂ was like adding a heater in the atmosphere, which
663 triggered a SW circulation anomaly thus resulted in a slump in LW speed. The decrease of SST at a
664 large scale further boosted the decrease of LW speed. The slumps in both SLB speed and SLB day
665 number could help to accumulate the local aerosols (Shen and Zhao, 2020), which further catalyzed the
666 physical processes mentioned in the mechanism and finally formed a positive feedback mechanism
667 under a scenario of mega fires.

668 Essentially, narrowed TDLS was the direct cause of SLB speed decrease, which was affected by
669 various factors in the form of either shortwave radiation or longwave radiation. It not only weakened
670 the SLB speed, but also brought about a slump in SLB day number. The *in situ* radiation, including
671 both longwave and shortwave radiation reaching the ground, has a direct impact on the TDLS
672 considering the basic physical mechanism of SLB formation. Note that the specific weather condition,
673 cloud fraction, COD, and the type of clouds and aerosols could all affect the *in situ* radiation. Apart



674 from *in situ* radiation, the heat release in urban areas, heat waves, heating effect of nearby heat sources,
675 large-scale signals of SST and land surface temperature variation could all affect TDLS by changing
676 either the local land temperature or SST. The large-scale signals of temperature variations could be
677 caused by either natural variability or human variability. Normally, SLB forms when the TDLS is
678 obvious and the background wind field is mild. So the condition of large scale wind field such as
679 monsoon is also an important influencing factor of SLB. Apart from the slump in both SLB day
680 number and LW speed during mega fire events, there were fluctuations in both of their trends, which is
681 need further study in future.

682 **Data availability.** The Dynamic Land Cover Dataset (DLCD) can be approached through Geoscience
683 Australia (<http://www.ga.gov.au/scientific-topics/earth-obs/accessing-satellite-imagery/landcover>,
684 Lymburner et al., 2015). MERRA-2 Reanalysis data can be approached through the NASA Global
685 Modeling and Assimilation Office (<https://gmao.gsfc.nasa.gov/reanalysis/MERRA-2/>, Global Modeling
686 and Assimilation Office (GMAO), 2015). MODIS observation data can be approached through
687 Earthdata center managed by NOAA (<https://earthdata.nasa.gov/search?q=MCD06>). GDAS data used
688 in HYSPLIT data are accessible through the NOAA READY website (<http://www.ready.noaa.gov>,
689 NOAA, 2016). Fire spot and FRP data can be approached from MODIS MCD14 product managed by
690 NOAA (<https://earthdata.nasa.gov/search?q=MCD14>). The wind and temperature observation data
691 from NOAA global observation network can be approached by NOAA's official website
692 (<http://www1.ncdc.noaa.gov/pub/data/noaa/>). The ERA5 data can be approached through official
693 website of Copernicus project (<https://climate.copernicus.eu/climate-reanalysis>).

694 **Author contributions.** CFZ and LXS developed the ideas and designed the study. LXS, XCY, YKY and
695 PZ contributed to collection and analyses of data. LXS and XCY performed the analysis and prepared
696 the manuscript. CFZ supervised and modified the manuscript. All authors made substantial
697 contributions to this work.

698 **Competing interests.** The authors declare that they have no conflict of interest.



699 **Acknowledgements.** This work was supported by the Ministry of Science and Technology of China
700 National Key Research and Development Program (2019YFA0606803), the National Natural Science
701 Foundation of China (41925022), the State Key Laboratory of Earth Surface Processes and Resources
702 Ecology, and the Fundamental Research Funds for the Central Universities.

703 Reference

- 704 Albrecht, B. A.: Aerosols, Cloud Microphysics, and Fractional Cloudiness, *Science*, 245, 1227–1230,
705 <https://doi.org/10.1126/science.245.4923.1227>, 1989.
- 706 Cao, L. Z., Chen, X., Zhang, C., Kurban, A., Yuan, X. L., Pan, T., and Maeyer, P.: The temporal and
707 spatial distributions of the near-surface CO₂ concentrations in central Asia and analysis of their
708 controlling factors, *Atmosphere*, 8, 1–14, <http://doi.org/10.3390/atmos8050085>, 2017.
- 709 Charlson, R. J., Schwartz, S. E., Hales, J. M., Cess, R. D., Coakley, J. A., Hansen, J. E., and Hofmann,
710 D. J.: Climate forcing by anthropogenic aerosols, *Science*, 255, 423–430, 1992.
- 711 Chuang, C. C., Penner, J. E., Prospero, J. M., Grant, K. E., Rau, G. H., and Kawamoto, K.: Cloud
712 susceptibility and the first aerosol indirect forcing: Sensitivity to black carbon and aerosol
713 concentrations, *J. Geophys. Res.-Atmos.*, 107, 4564, <https://doi.org/10.1029/2000JD000215>,
714 2002.
- 715 Cuxart, J., Jiménez, M.A., Prtenjak, M.T., and Grisogono, B.: Study of a sea-breeze case through
716 momentum, temperature, and turbulence budgets, *J. Appl. Meteorol. Climatol.*, 53, 2589–2609,
717 2014.
- 718 Garrett, T. J. and Zhao, C.: Increased Arctic cloud longwave emissivity associated with pollution from
719 mid-latitudes, *Nature*, 440, 787–789, <https://doi.org/10.1038/nature04636>, 2006.
- 720 Giglio, L., Schroeder, W., and Justice, C. O.: The collection 6 MODIS active fire detection algorithm
721 and fire products, *Remote Sens. Environ.*, 178, 31–41, <https://doi.org/10.1016/j.rse.2016.02.054>,
722 2016.
- 723 Grandey, B. S., Lee, H. H., and Wang, C.: Radiative effects of interannually varying vs. interannually
724 invariant aerosol emissions from fires, *Atmos. Chem. Phys.*, 16, 14495–14513,
725 <https://doi.org/10.5194/acp-16-14495-2016>, 2016.
- 726 Han, W. C., Li, Z. Q., Wu, F., Zhang, Y., and Lee, S. S.: Opposite effects of aerosols on daytime urban



- 727 heat island intensity between summer and winter, *Atmos. Chem. Phys.*, 20, 6479–6493,
728 <https://doi.org/10.5194/acp-2020-162>, 2020.
- 729 Hirsch, E., and Koren, I.: Record-breaking aerosol levels explained by smoke injection into the
730 stratosphere, *Science*, 371, 1269-1274, <http://doi.org/10.1126/science.abe1415>, 2021.
- 731 Intergovernmental Panel on Climate Change, *Climate Change 2013: The Physical Science Basis.*
732 *Contribution of Working Group I to the Fifth Assessment Report of the Intergovernmental Panel*
733 *on Climate Change*, 1535 pp, Cambridge Univ. Press, Cambridge, U. K., and New York, 2013.
- 734 Jacobson, M. Z. : Strong radiative heating due to the mixing state of black carbon in atmospheric
735 aerosols, *Nature*, 409, 695-697, 2001.
- 736 Jacobson, M. Z.: Effects of biomass burning on climate, accounting for heat and moisture fluxes, black
737 and brown carbon, and cloud absorption effects, *J. Geophys. Res.-Atmos.*, 119, 8980–9002,
738 <https://doi.org/10.1002/2014jd021861>, 2014.
- 739 Jia, S. Q., Jing, J. L., Ju, E. D., and Chi, W. B.: Discussions on the temperature and pressure fields in a
740 mega forest fire zone, *J. Nort. Fore. Uni.*, 15, 226-232,
741 <http://doi.org/10.13759/j.cnki.dlxb.1987.s4.028>, 1987.
- 742 Kloss, C., Berthet, G., Sellitto, P., Ploeger, F., Bucci, S., Khaykin, S., Jégou, F., Taha, G., Thomason, L.
743 W., Barret, B., Flochmoen, E., Hobe, M., Bossolasco, A., Bègue, N., and Legras, B.: Transport of
744 the 2017 Canadian wildfire plume to the tropics via the Asian monsoon circulation, *Atmos. Chem.*
745 *Phys.*, 19, 13547–13567, <https://doi.org/10.5194/acp-19-13547-2019>, 2019.
- 746 Kusaka, H., Kimura, F., Hirakuchi, H., and Mizutori, M.: The effects of land-use alteration on the sea
747 breeze and daytime heat island in the Tokyo metropolitan area, *J. Meteorol. Soc. Jpn.*, 78,
748 405–420, https://doi.org/10.2151/jmsj1965.78.4_405, 2000.
- 749 Li, J. W., Yang, L. Q., Li, X. W., and Zheng, H. R.: Visualization of local wind field based forest-fire's
750 forecast modeling for transportation planning, *Multimed. Tools. Appl.*, 1, 1-15,
751 <http://doi.org/10.1007/s11042-016-3357-7>, 2016.
- 752 Luhar, A. K., Mitchell, R. M., Meyer, C. P., Qin, Y., Campbell, S., Gras, J. L., and Parry, D.: Biomass
753 burning emissions over northern Australia constrained by aerosol measure-
754 ments: II—Model validation, and impacts on air quality and radiative forcing, *Atmos. Environ.*, 42,
755 1647–1664, <https://doi.org/10.1016/j.atmosenv.2007.12.040>, 2008.
- 756 Lyburner, L., Tan, P., McIntyre, A., Thankappan, M., and Sixsmith, J.: Dynamic Land Cover Dataset



757 Version 2.1. Geoscience Australia, Canberra, available at:
758 <http://pid.geoscience.gov.au/dataset/ga/83868> (last access: 31 January 2021), 2015.

759 Ma, Y., Gao, R. Z., and Miao, S. G.: Impacts of urbanization on summer-time SLB circulation in
760 Qingdao, *Acta. Sci. Circumst.*, 33, 1690–1696, <https://doi.org/10.13671/j.hjkxxb.2013.06.030>,
761 2013.

762 Mallet, M. D., Desservettaz, M. J., Miljevic, B., Milic, A., Ristovski, Z. D., Alroe, J., Cravigan, L. T.,
763 Jayaratne, E. R., PatonWalsh, C., Griffith, D. W. T., Wilson, S. R., Kettlewell, G., vander Schoot,
764 M. V., Selleck, P., Reisen, F., Lawson, S. J., Ward, J.,
765 Harnwell, J., Cheng, M., Gillett, R. W., Molloy, S. B., Howard, D., Nelson, P. F., Morrison, A. L.,
766 Edwards, G. C., Williams, A. G., Chambers, S. D., Werczynski, S., Williams, L. R., Winton, V. H.
767 L., Atkinson, B., Wang, X., and Keywood, M. D.: Biomass burning emissions in north Australia
768 during the early dry season: an overview of the 2014 SAFIRED campaign, *Atmos. Chem. Phys.*,
769 17, 13681–13697, <https://doi.org/10.5194/acp-17-13681-2017>, 2017.

770 McCoy, D. T., and Hartmann, D. L.: Observations of a substantial cloud-aerosol indirect effect during
771 the 2014–2015 Bárðarbunga-Veiðivötnfissure eruption in Iceland, *Geophys. Res. Lett.*, 42,
772 10409–10414, <http://doi.org/10.1002/2015GL067070>, 2015.

773 Meyer, C. P., Luhar, A. K., and Mitchell, R. M.: Biomass burning emissions over northern Australia
774 constrained by aerosol measurements: I – Modelling the distribu-
775 tion of hourly emissions, *Atmos. Environ.*, 42, 1629–1646,
776 <https://doi.org/10.1016/j.atmosenv.2007.10.089>, 2008.

777 Miller, S. T. K., Keim, B. D., Talbot, R. W., and Mao, H.: Sea breeze: Structure, forecasting, and
778 impacts, *Rev. Geophys.*, 41, 1011, <http://doi:10.1029/2003RG000124>, 2013.

779 Mitchell, R. M., Forgan, B. W., Campbell, S. K., and Qin, Y.: The climatology of Australian tropical
780 aerosol: Evidence for regional correlation, *Geophys. Res. Lett.*, 40, 2384–2389,
781 <https://doi.org/10.1002/grl.50403>, 2013.

782 Mitchell, R. M., O'Brien, D. M., and Campbell, S. K.: Characteristics and radiative impact of the
783 aerosol generated by the Canberra firestorm of January 2003, *J. Geophys. Res.-Atmos.*, 111,
784 D02204, <https://doi.org/10.1029/2005jd006304>, 2006.

785 Nai, F. B., Zhao, L. N., and Wu, J. R.: Impacts of sea-land and mountain-valley circulations on the air
786 pollution in Beijing-Tianjin-Hebei: a case study, *Environ. Pollut.*, 234, 429–438,



- 787 <https://doi.org/10.1016/j.envpol.2017.11.066>, 2018.
- 788 Ohneiser, K., Ansmann, A., Baars, H., Seifert, P., Barja, B., Jimenez, C., Radenz, M., Teisseire, A.,
789 Floutsi, A., Haarig, M., Foth, A., Chudnovsky, A., Engelmann, R., Zamorano, F., Bühl, J., and
790 Wandinger, U.: Smoke of extreme Australian bushfires
791 observed in the stratosphere over Punta Arenas, Chile, in January 2020: optical thickness, lidar ratios,
792 and depolarization ratios at 355 and 532nm, *Atmos. Chem. Phys.*, 20, 8003–8015,
793 <https://doi.org/10.5194/acp-20-8003-2020>, 2020.
- 794 Portin, H., Mielonen, T., Leskinen, A., Arola, A., Pärjälä, E., Romakkaniemi, S., Laaksonen, A.,
795 Lehtinen, K. E. J., and Komppula, M.: Biomass burning aerosols observed in Eastern Finland
796 during the Russian wildfires in summer 2010 e Part 1: In-situ aerosol characterization, *Atmos.*
797 *Environ.*, 47, 269-278, <http://doi:10.1016/j.atmosenv.2011.10.067>, 2012.
- 798 Ramana, M. V., Ramanathan, V., Feng, Y., Yoon, S. C., Kim, S. W., Carmichael, G. R., and Schauer, J.
799 J.: Warming influenced by the ratio of black carbon to sulphate and the black-carbon source,
800 *Nature. Geosci.*, 1, 542-545, <http://doi.org/10.1038/NGEO918>, 2010.
- 801 Rajib, P., and Heekwa, L.: Estimation of the effective zone of sea/land breeze in a coastal area, *Atmos.*
802 *Pollut. Res.*, 2, 106–115, <https://doi.org/10.5094/APR.2011.013>, 2010.
- 803 Sarker, A., Saraswat, R. S., Chandrasekar, A.: Numerical study of the effects of urban heat island on the
804 characteristic features of the sea breeze circulation, *J. Earth Syst. Sci.*, 107, 127–137, 1998.
- 805 Shen, L. X., Zhao, C. F., Ma, Z. S., Li, Z. Q., Li, J. P., and Wang, K. C.: Observed decrease of summer
806 sea-land breeze in Shanghai from 1994 to 2014 and its association with urbanization, *Atmos. Res.*,
807 227, 198-209, <http://doi.org/10.1016/j.atmosres.2019.05.007>, 2019.
- 808 Shen, L. X., and Zhao, C. F.: Dominance of Shortwave Radiative Heating in the Sea - Land Breeze
809 Amplitude and its Impacts on Atmospheric Visibility in Tokyo, Japan, *J. Geophys. Res.-Atmos.*,
810 125, 1-19, <https://doi.org/10.1029/2019jd031541>, 2020.
- 811 Shen, L. X., Zhao, C. F., and Yang, X. C.: Insight Into the Seasonal Variations of the Sea-Land Breeze
812 in Los Angeles With Respect to the Effects of Solar Radiation and Climate Type, *J. Geophys.*
813 *Res.-Atmos.*, 126, 1-21, <https://doi.org/10.1029/2019jd033197>, 2021.
- 814 Shen, L. X., Zhao, C. F., and Yang, X. C.:
815 Climate-Driven Characteristics of Sea-Land Breezes Over the Globe, *Geophys. Res. Lett.*, 48,
816 1-10, <https://doi.org/10.1029/2020GL092308>, 2021.



- 817 Stageberg, M. S.: Sensitivities of simulated fire-induced flows to fire shape and background wind
818 profile using a cloud-resolving model, Master Dissertation, Michigan State University, ProQuest
819 Dissertations Publishing, 10816178, 2018.
- 820 Torres, O., Jethva, H., Ahn, C., Jaross, G., and Loyola, D. G.: TROPOMI aerosol products: evaluation
821 and observations of synoptic-scale carbonaceous aerosol plumes
822 during 2018–2020, *Atmos. Meas. Tech.*, 13, 6789–6806, <https://doi.org/10.5194/amt-13-6789-2020>,
823 2020.
- 824 Turnock, S. T., Spracklen, D. V., Carslaw, K. S., Mann, G. W., Woodhouse, M. T., Forster, P. M.,
825 Haywood, J., Johnson, C. E., Dalvi, M., Bellouin, N., and Sanchez-Lorenzo, A.: Modelled and
826 observed changes in aerosols and surface solar radiation over Europe between 1960 and 2009,
827 *Atmos. Chem. Phys.*, 15, 9477–9500, <https://doi.org/10.5194/acp-15-9477-2015>, 2015.
- 828 van der Werf, G. R., Randerson, J. T., Giglio, L., Collatz, G. J., Kasibhatla, P. S., and Arellano Jr., A. F.:
829 Interannual variability in global biomass burning emissions from 1997 to 2004, *Atmos. Chem.*
830 *Phys.*, 6, 3423–3441, <https://doi.org/10.5194/acp-6-3423-2006>, 2006.
- 831 Vermote, E., Ellicott, E., Dubovik, O., Lapyonok, T., Chin, M., Giglio, L., and Roberts, G. J.: An
832 approach to estimate global biomass burning emissions of organic and black carbon from MODIS
833 fire radiative power, *J. Geophys. Res.-Atmos.*, 114, D18205,
834 <https://doi.org/10.1029/2008jd011188>, 2009.
- 835 Walcek, C. J.: Effects of wind shear on pollution dispersion, *Atmos. Environ.*, 36, 511–517,
836 [http://doi.org/10.1016/s1352-2310\(01\)00383-1](http://doi.org/10.1016/s1352-2310(01)00383-1), 2002.
- 837 Wang, Y., Jiang, J. H., and Su, H.: Atmospheric responses to the redistribution of anthropogenic
838 aerosols, *J. Geophys. Res.-Atmos.*, 120, 9625–9641, <http://doi.org/10.1002/2015JD023665>, 2015.
- 839 Xue, D. Q., Zheng, Q. L., and Qian, X. Z.: Features of sea-land circulation with its influence over
840 Shandong Peninsula, *J. Nanjing Inst. Meteorol.*, 18, 293–299,
841 <https://doi.org/10.13878/j.cnki.dqkxxb.1995.02.021>, 1995.
- 842 Yan, H., and Anthes, R. A.: The effect of latitude on the sea breeze, *Mon. Wea. Rev.*, 115, 936–956,
843 1987.
- 844 Yang, X., Zhao, C. F., Zhou, L., Wang, Y., and Liu, X.: Distinct impact of different types of aerosols on
845 surface solar radiation in China, *J. Geophys. Res. Atmos.*, 121, 6459–6471,
846 <http://doi.org/10.1002/2016JD024938>, 2016.



- 847 Yang, X. C., Zhao, C. F., Yang, Y. K., Yan, X., and Fan, H.: Statistical aerosol properties associated
848 with fire events from 2002 to 2019 and a case analysis in 2019 over Australia, *Atmos. Chem.*
849 *Phys.*, 21, 3833–3853, <https://doi.org/10.5194/acp-21-3833-2021>, 2021.
- 850 Zhang, H., Wang, Z. L., and Zhao, S. Y.: Atmospheric aerosols and their climatological effect, China
851 Meteorological Press, Beijing, China, ISBN: 978-7-5029-6676-8, 2017.
- 852 Zhao, C., Lin, Y., Wu, F., Wang, Y., Li, Z., Rosenfeld, D., and Wang, Y.: Enlarging rainfall area of
853 tropical cyclones by atmospheric aerosols, *Geophys. Res. Lett.*, 45, 8604-8611,
854 <http://doi.org/10.1029/2018GL079427>, 2018.
- 855 Zhao, C. F., Yang, Y. K., Fan, H., Huang, J. P., Fu, Y. F., Zhang, X. Y., Kang, S. C., Cong, Z. Y., Husi,
856 L., and Menenti, M.: Aerosol characteristics and impacts on weather and climate over Tibetan
857 Plateau, *Nat. Sci. Rev.*, 7, 492-495, <http://doi.org/10.1093/nsr/nwz184>, 2020.
- 858 Zhu, L., Meng, Z., Zhang, F., and Markowski, P. M.: The influence of sea- and land-breeze circulations
859 on the diurnal variability in precipitation over a tropical island, *Atmos. Chem. Phys.*, 17,
860 13213–13232, <https://doi.org/10.5194/acp-17-13213-2017>, 2017.

861 **Figures and tables**

862 Table 1: Summary of information for the verification of OE-SLB at Brisbane Archerfield.

The range of SW	The range of LW	PTS (UTC)	PTL (UTC)
[20° 135°]	[200° 315°]	[500 800]	[1400 2000]

863

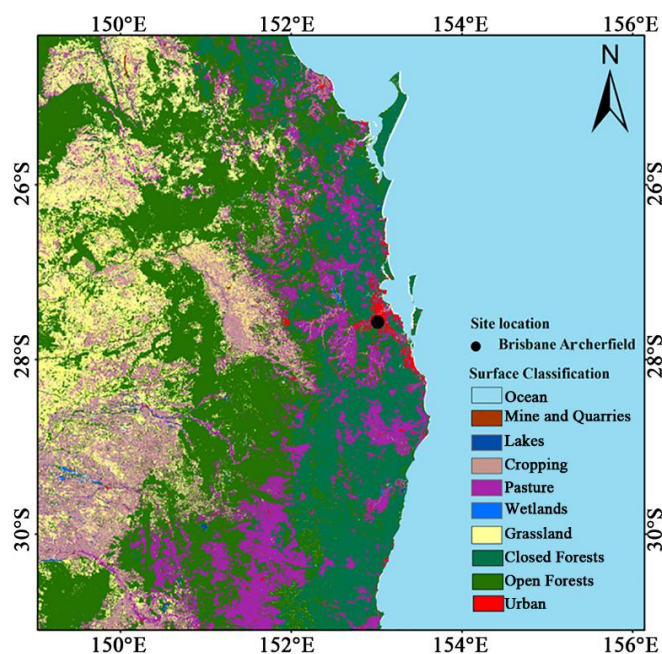
864 Table 2: Summary on the effect of different factors on TDLS. Factors marked in red represent that
865 they are either weak factor or potential factor derived from theoretical analysis but not verified by
866 observation.

Influencing factors		Forcing on Daytime TDLS	Forcing on Nighttime TDLS
Large scale forcing	Cooling of SST on a large scale (Hirsch and Koren, 2021)	+	-
Regional forcing	Heating effect of nearby	+	-



fire spots		
Total aerosols	-	×
BC	+	-
OC	-	×
CO ₂	+	-

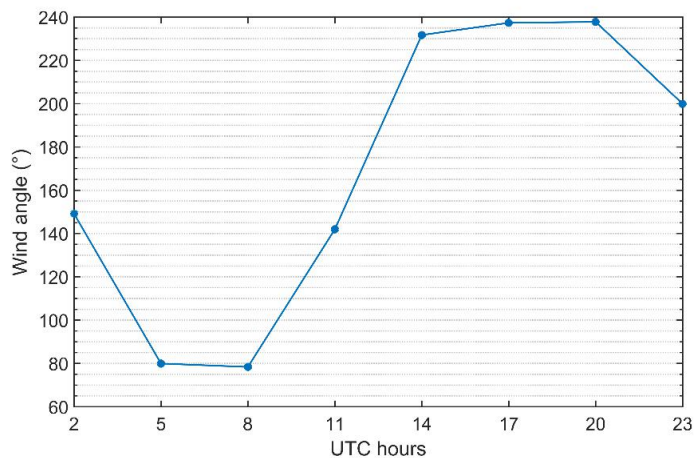
867



868

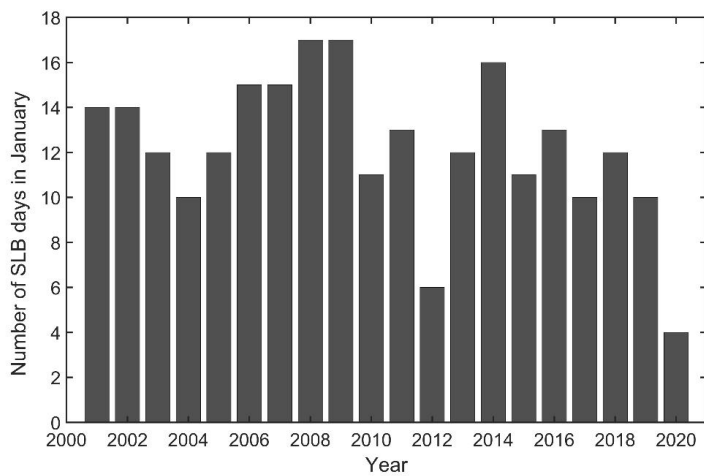
869 Figure 1: The map of eastern Australia with land-cover types. The observation site is marked in a black

870 dot.



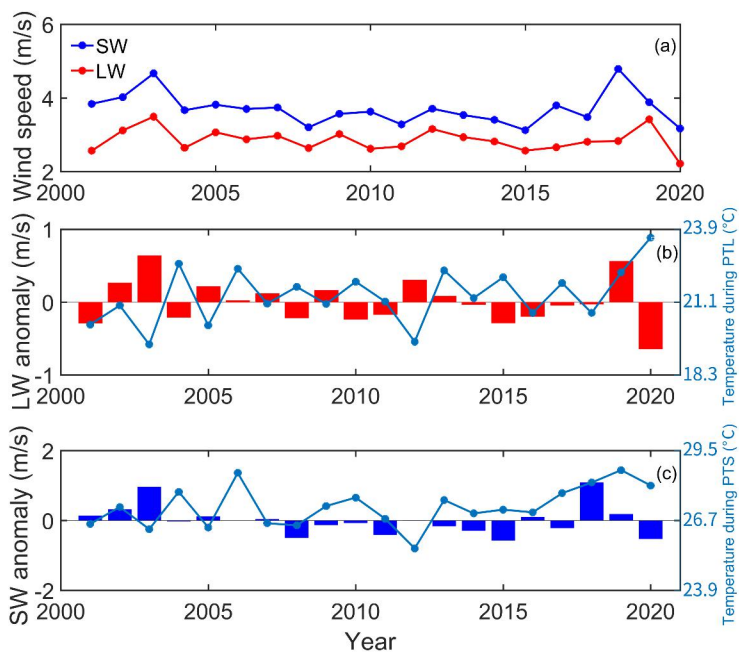
871

872 Figure 2: Hourly average of wind angle in a diurnal period (HAWADP) of the local wind.



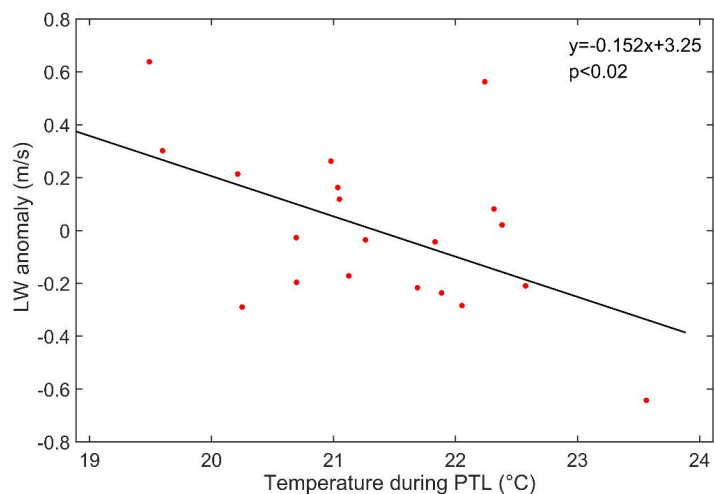
873

874 Figure 3: Number of SLB days in January from 2001 to 2020.



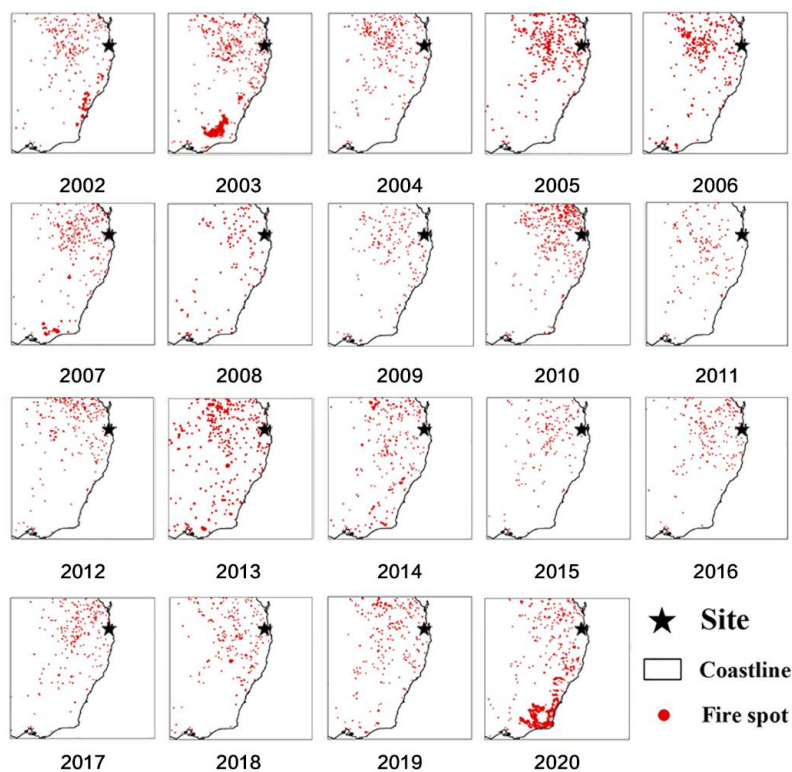
875

876 Figure 4: The trends of SW and LW speeds (a), the LW speed anomaly and land temperature during
877 nighttime (b), the SW speed anomaly and land temperature during daytime (c) based on the monthly
878 average of them during January from 2001 to 2020.



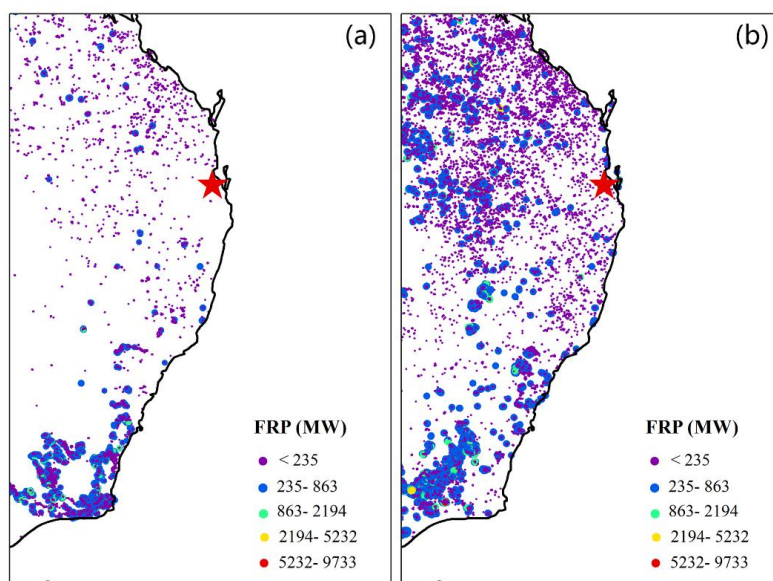
879

880 Figure 5: The relationship between LW anomaly and temperature during PTL based on monthly
881 average of them during January from 2001 to 2020.



882

883 Figure 6: The fire spot distribution in the eastern Australia during January from 2002 to 2020.

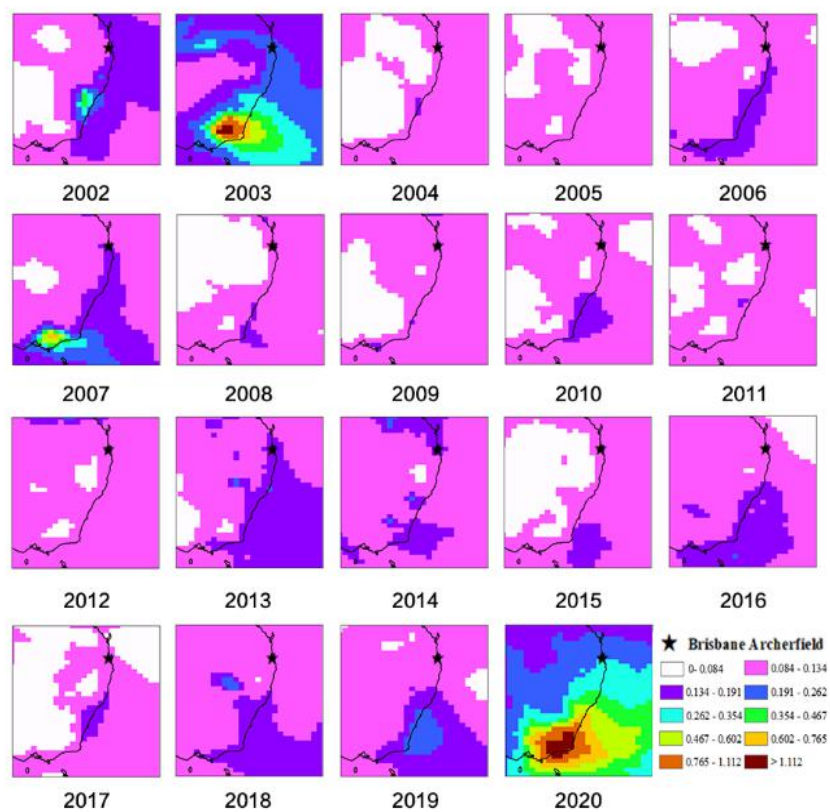


884

885 Figure 7: The fire radiative power (FRP) of total fire spots in eastern Australia during January in 2020



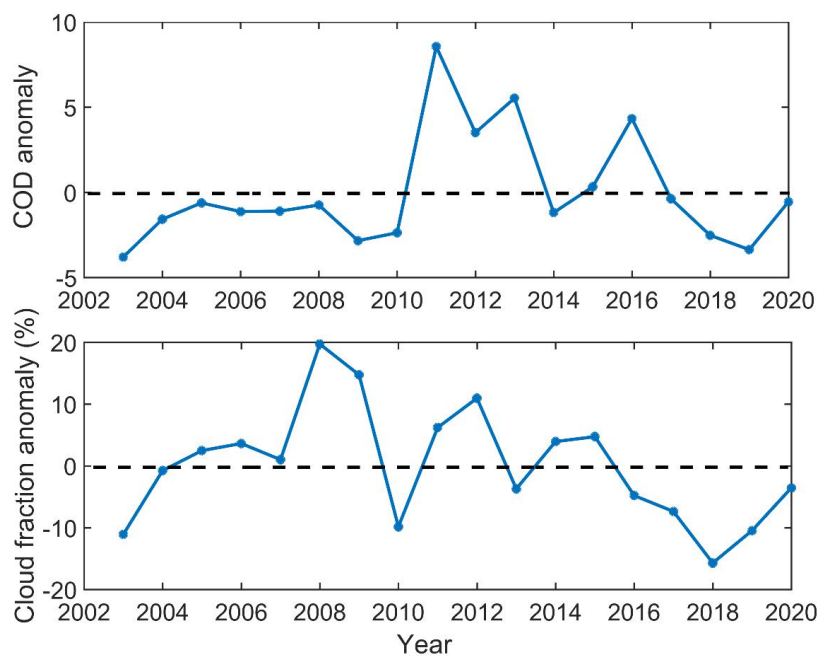
886 (a), January from 2002 to 2019 (b).



887

888 Figure 8: The spatial distribution of aerosol optical depth (AOD) of total aerosols in eastern Australia

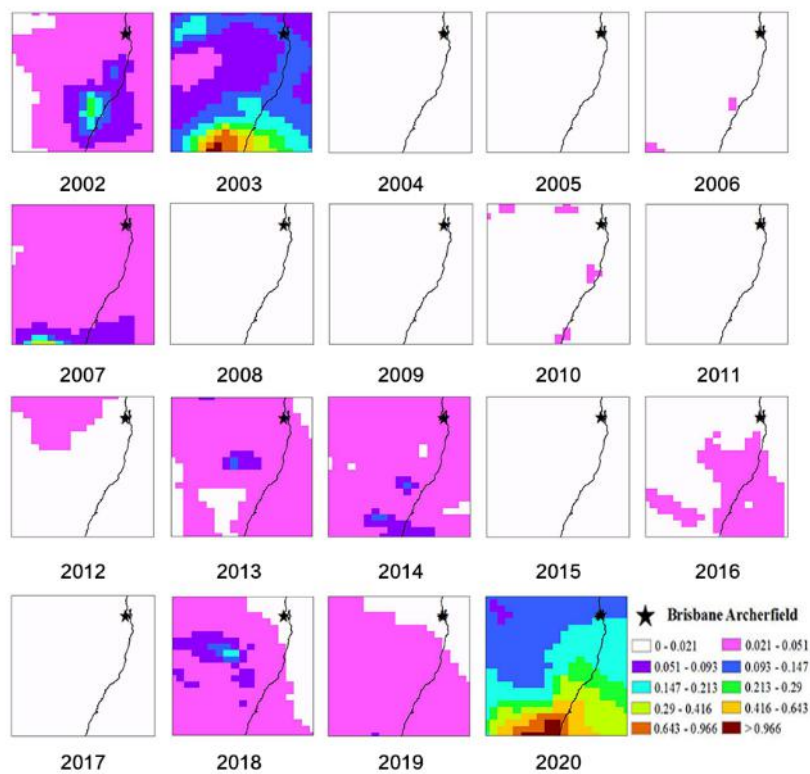
889 during January from 2002 to 2020.



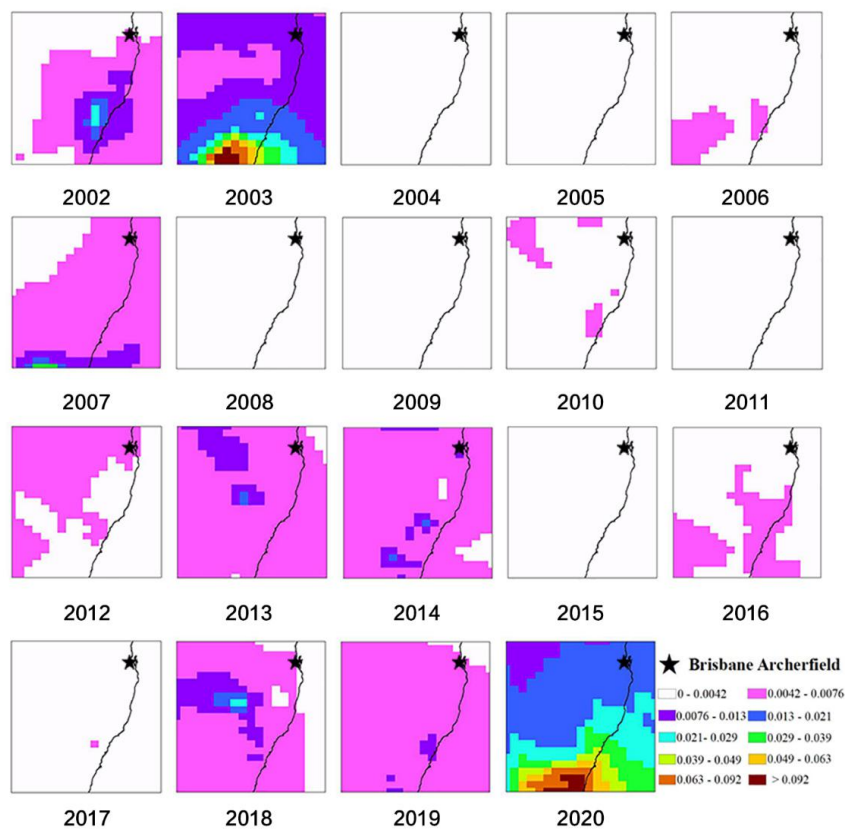
890

891 Figure 9: The monthly cloud optical depth (COD) anomaly and cloud fraction anomaly at Brisbane

892 Archerfield during January from 2003 to 2020.



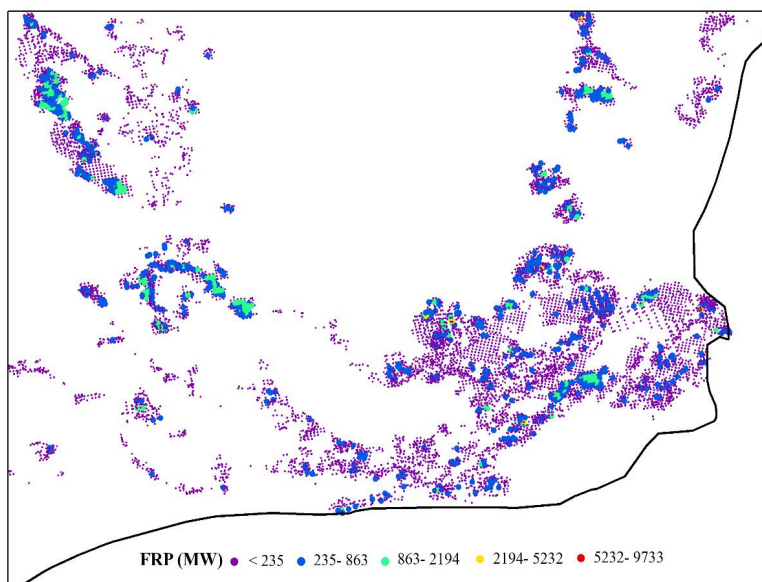
893
894 Figure 10: The spatial distribution of aerosol optical depth (AOD) of organic carbon (OC) in eastern
895 Australia during January from 2002 to 2020.



896

897 Figure 11: The spatial distribution of aerosol optical depth (AOD) of black carbon (BC) in eastern

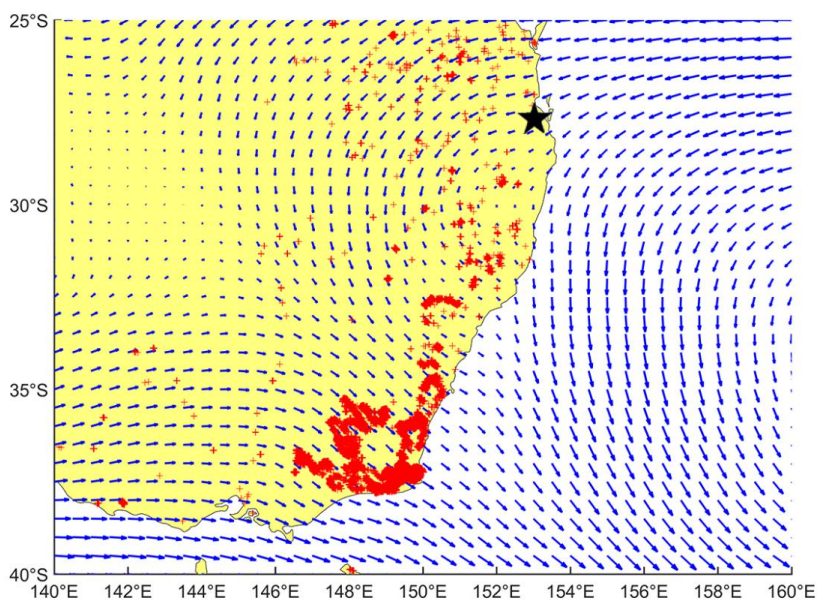
898 Australia during January from 2002 to 2020.



899

900 Figure 12: The detailed distribution of fire spots and their FRP in the fire center during January in

901 2020.



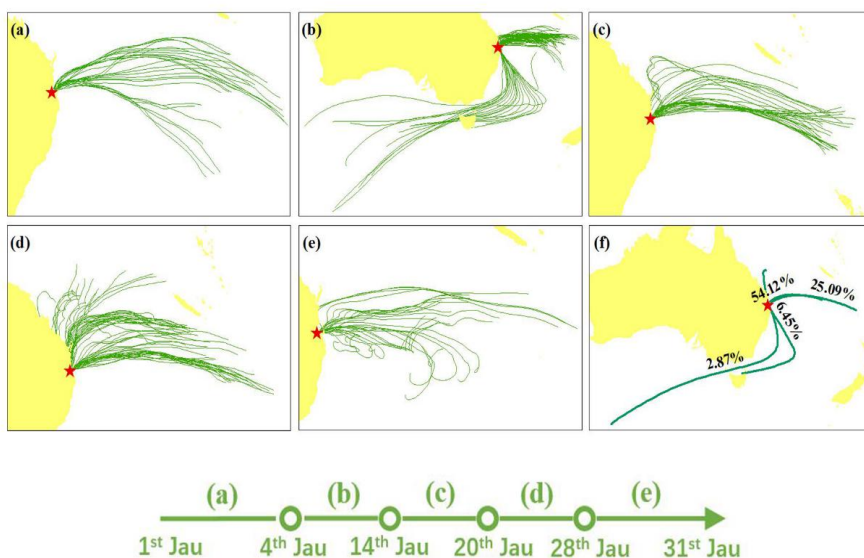
902

903 Figure 13: Monthly average background wind field based on wind information at pressure levels from

904 100hPa to 700hPa in January 2020. The red crosses present fire spots and the black star represents the

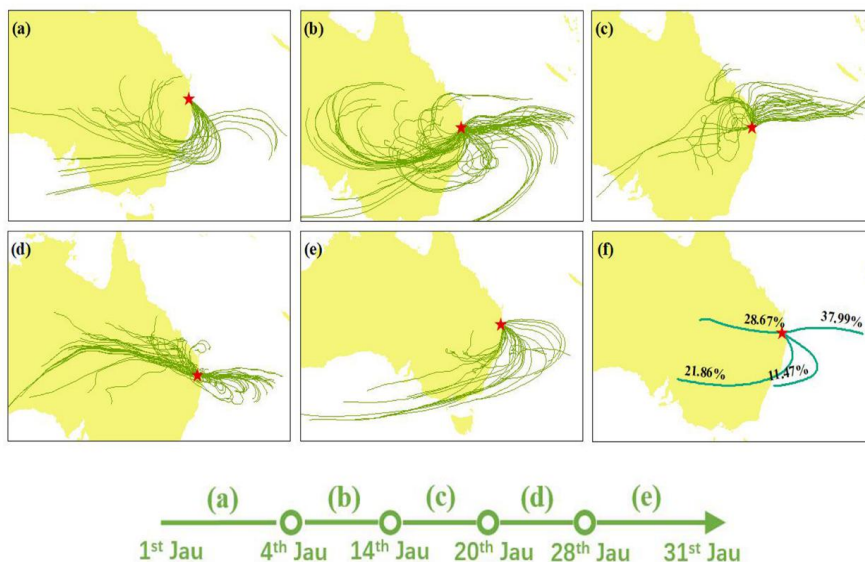


905 site location.

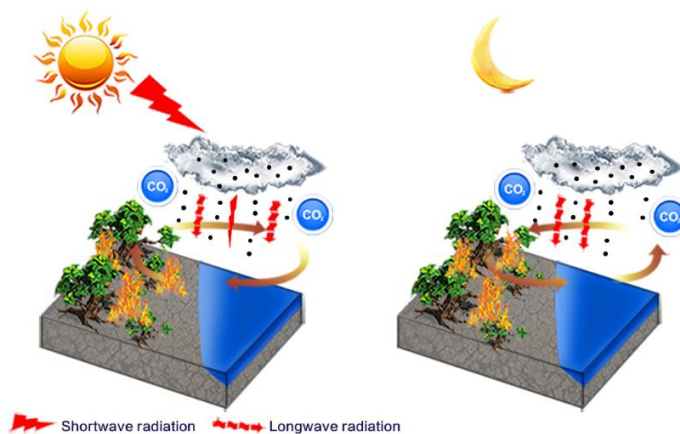


906

907 Figure 14: The site's the wind backward trajectories at 500 m during January in 2020. The wind
908 backward trajectories during first No-SLB period from 1st Jau to 3th Jau (a), the wind backward
909 backward trajectories during second No-SLB period from 5th Jau to 13th Jau (b), the wind backward trajectories
910 during third No-SLB period from 15th Jau to 19th Jau (c), the wind backward trajectories during fourth
911 No-SLB period from 21st Jau to 27th Jau (d), the wind backward trajectories during fifth No-SLB
912 period from 29th Jau to 31st Jau (e), the contribution of four main wind clusters based on the wind
913 backward trajectories during the whole month of January in 2020 (f).



914
 915 Figure 15: The site's the wind backward trajectories at 3 km during January in 2020. The wind
 916 backward trajectories during first No-SLB period from 1st Jau to 3th Jau (a), the wind backward
 917 trajectories during second No-SLB period from 5th Jau to 13th Jau (b), the wind backward trajectories
 918 during third No-SLB period from 15th Jau to 19th Jau (c), the wind backward trajectories during fourth
 919 No-SLB period from 21st Jau to 27th Jau (d), the wind backward trajectories during fifth No-SLB
 920 period from 29th Jau to 31st Jau (e), the contribution of four main wind clusters based on the wind
 921 backward trajectories during the whole month of January in 2020 (f).



922
 923 Figure 16: The summary of mechanisms containing influencing factors of local SLB during daytime



924 and nighttime. The black dots represent aerosols which include both scattering aerosols and absorptive
925 aerosols. The width of arrows of 'shortwave radiation' represents the magnitude of shortwave radiation.